Supplementary Material

Sodium Alginate Based Skin-Core Fibers with Profoundly Enhanced Moisture-Electric Generation Performance and their Multifunctionality

Rui Zhang, Meijie Qu, Hai Wang*, Shuhui Li, Yutong Song, Ping Tang, Yuezhen Bin*

Department of Polymer Science and Engineering, School of Chemical Engineering, Dalian University of Technology, Dalian 116024, PR China

*Corresponding authors.

E-mail addresses: haiwang@dlut.edu.cn (H. Wang), binyz@dlut.edu.cn (Y. Bin).

1 Characterization

Mechanical properties of fibers were measured by a TST250V Linkam extensometer (Linkam, U.K.) at 25 ℃ and a deformation rate of 200 μm/s. The original length was 15 mm in all tests.

Wide angle X-ray diffraction (WAXD) and small angle X-ray scattering (SAXS) measurements were conducted using a Rigaku NANOPIX X-ray WAXD/SAXS system equipped with a Rigaku Hypix 6000 HPC detector (Rigaku, Japan). Cu-Kα line (λ = 1.54 Å) was used as the incident beam. The camera distance of the WAXD and SAXS measurement was 86 and 650 mm, respectively.

The morphology of fibers was observed using a NOVA NanoSEM 450 scanning electron microscope (FEI, USA). Fibers in observation were epoxy-coated for brittle fracture to obtain a neat cross-section. The surface and cross-section of fibers for measurement were sprayed with gold.

The resistance of all fibers was measured using two wires mode using a 2450 digital source meter (Keithley, USA). Each fiber was measured five times.

The moist-electric output voltage and current of SA/PEDOT:PSS fibers after drying were collected using a 2450 digital source meter (Keithley, USA). The humidity environment was regulated using a home-made humidity control system. The humidity control system in wet mode maintained RH = 95% using N_2 to carry moisture, and the dry mode maintained RH = 5% using continuous high purity N_2.

The thermoelectric output voltages and currents of SA/PEDOT:PSS were also collected using a 2450

digital source meter (Keithley, USA). Temperature gradient on the FTEG devices was constructed using a warm water bottle and hot plate at ambient temperature, and the temperature difference (ΔT) between the two ends of FTEG devices was monitored using a DT-3891G temperature indicator (Huashengchang, China).

Joule heating performance was tested by applying different voltages to the two ends of the SA/PEDOT:PSS fiber (the same electrode connection as FTEG) using a RXN-303D DC regulated power supplies (Zhaoxin, China). The temperature change of the fiber was recorded using a 340 portable IR imager (FOTRIC, China).

2 Calculation

Power density: Power density is an important indicator of moist-electric and thermoelectric performance. The maximum output power density (P_{mo}) can be calculated using formulas (1).[1]

$$P_{mmo}=U_0^2/(S\times 4R_x) \quad (1)$$

P_{mmo}, U_0, R_x, and S represent the maximum output power density, the open circuit voltage, resistance of the matched load, sectional area of the fiber, respectively.

The thermoelectric power density is obtained using formula (2).

$$P_{Tmo}=U_0^2/(l\times D\times 4R_x) \quad (2)$$

P_{Tmo}, U_0, R_x, l, and D represent the maximum output power density, the voltage and resistance of the matched load, length, and diameter of the fiber, respectively.

Electrical Conductivity：The electrical conductivity of fiber can be calculated using formulas (3).

$$\sigma=4l/(R_0\times\pi\times D^2) \quad (3)$$

Herein, σ, l, R_0, and D represent electrical conductivity, length, internal resistance, and diameter of the fiber, respectively.

3 Supplementary Figures and tables

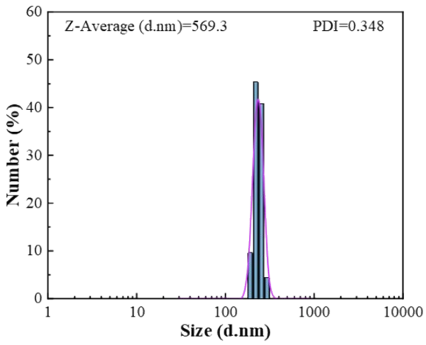

Fig. S1 Particle size distribution diagram of PEDOT:PSS aqueous dispersion

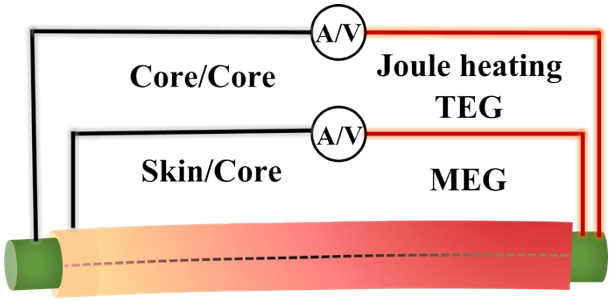

Fig. S2 Diagram of the different functions of Coax-P30% fiber with various wiring methods

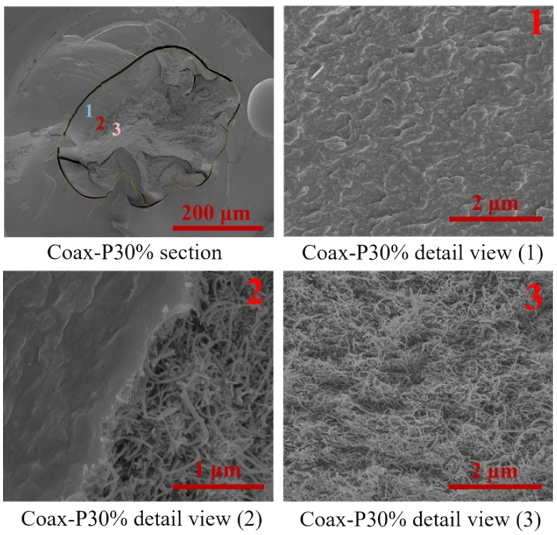

Fig. S3 SEM of Coax-P30% fiber section and detail view

The cross-section of Coax-P30% fiber is shown in Fig. S3. Position "1" and "3" represent the skin and core layer, respectively, which can be confirmed by the relative ratio of carbon to oxygen in the EDS energy spectrum of Fig. S4. The cross-section of the Coax-P30% fiber has an elliptical shape and its local magnification clearly shows the porous structure of MWCNT in the core layer due to the entanglement between the MWCNTs. In this study, SA/PEDOT:PSS and MWCNT were injected into the solidification

bath through cortex and core channels of the spinning needle, respectively, forming a two-phase structure. There is a clear interface between cortex and core in coaxial fiber (position "2"). The interaction involves van der Waals interaction between polymer and MWCNT and the insertion of MWCNT into polymer matrix.

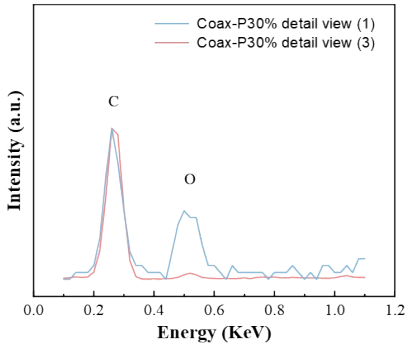

Fig. S4 EDS spectra of the Coax-P30% fiber skin and core layer

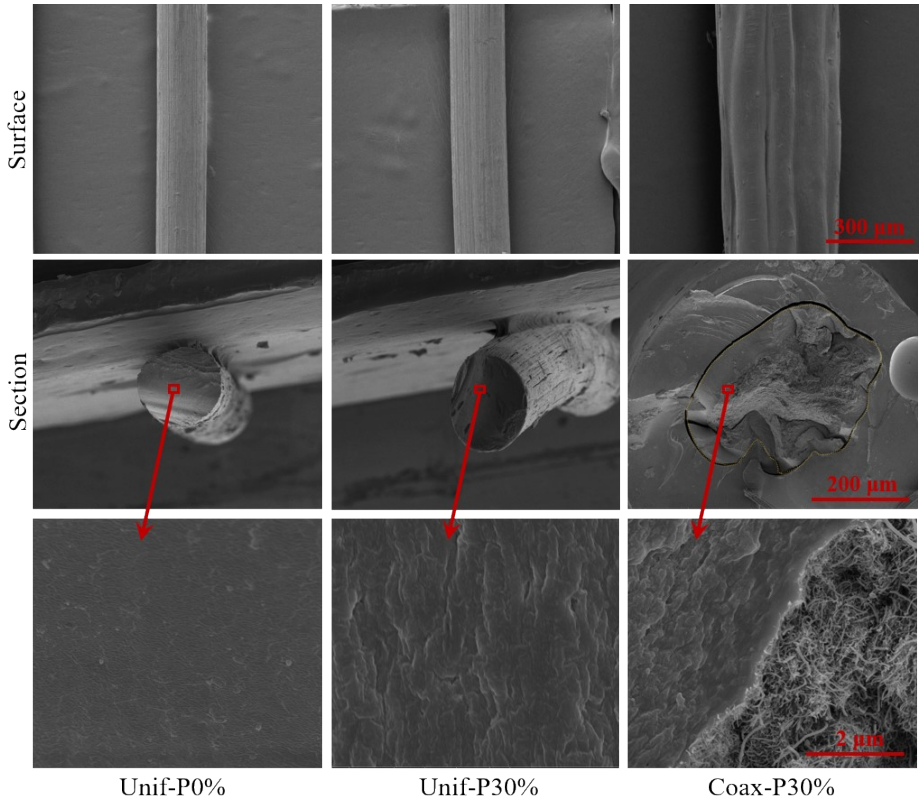

Fig. S5 SEM of Unif-P0%, Unif-P30% and Coax-P30% fiber surface and section

Compared to uniform fiber (Fig. S5), it can be found that coaxial fiber shows deeper and sparser grooves. This is due to the different solid content of the skin and core spinning solution of coaxial

SA/PEDOT:PSS fibers, which results in the inconsistent shrinkage of the skin and core layers during the drying process. In addition, a comparison of the cross-sections of coaxial fiber and uniform fiber shows that the introduction of PEDOT:PSS disrupts the regular aggregate of the long chain molecules of SA due to electrostatic complexation between PEDOT and PSS, judging from the rougher cross-sections of fibers with higher PEDOT:PSS composition.

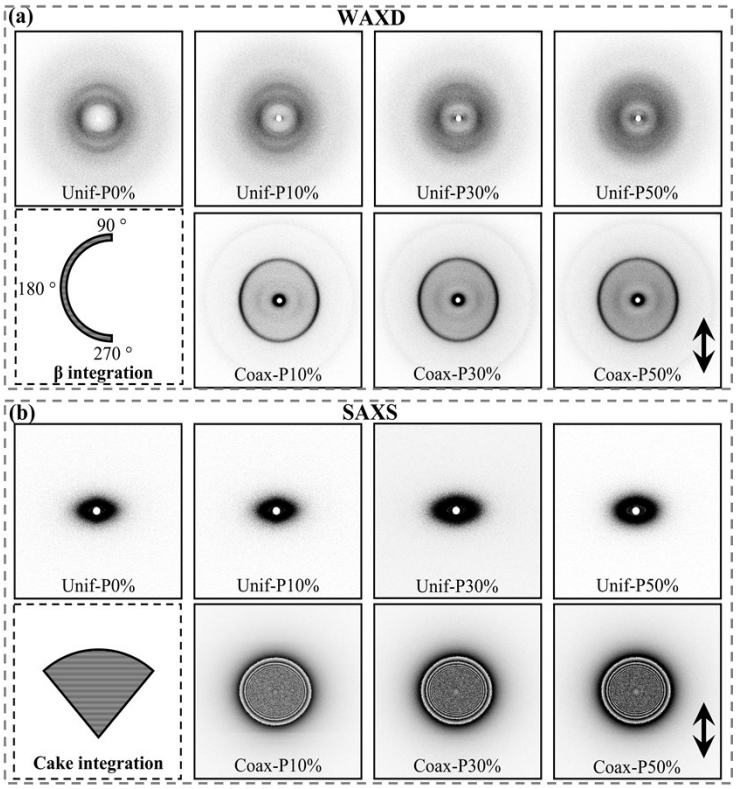

Fig. S6 The (a) 2D-WAXD and (b) 2D-SAXS curves of uniform fibers and coaxial fibers

The 2D-WAXD patterns of coaxial and uniform fibers are shown in Fig. S6(a). It can be observed that the intensity of the diffraction rings of coaxial and uniform fibers does not vary significantly with increasing PEDOT:PSS content. Fig. S7(a-b) show the 1D-WAXD curves for coaxial fibers and uniform fibers integrated in a circular fashion from the corresponding 2D-WAXD patterns. The 1D-WAXD curve of Unif-P0% fiber shows the characteristic peaks of SA at 2θ = 13.4° (110), and 20.4°. SA is usually a semi-crystalline polymer due to the strong intermolecular interactions between SA chains.[2-4] The 1D-WAXD curves of uniform fibers with PEDOT:PSS show the characteristic peaks of PEDOT:PSS at 2θ = 4.8° (100), 10.9° (200) and 25.0° (010),[5-6] the intensity of which increases with the increased PEDOT:PSS doping content. This implies a gradual increase of the crystallinity of uniform fiber. The 1D-WAXD curves for

coaxial fibers show the strong characteristic graphite peaks of MWCNT at 2θ = 25.2° (002) and 41.9° (100).[7] As thus, the diffractions of PEDOT:PSS are not obviously seen from the 1D-WAXD curves of Coax-fibers. But the effect of PEDOT:PSS content can be speculated from the mechanical and electric properties. In addition to this, anisotropic diffraction rings are observed on 2D-WAXD patterns of coaxial and uniform fibers, indicating that the (110) crystalline plane of SA in uniform and coaxial fibers and the (002) crystalline plane of MWCNT in coaxial fibers are preferentially oriented along the meridian direction. Fig. S7(c) show the orientation of the SA (110) crystal plane in coaxial and uniform fibers, and Fig. S7(d) show the orientation of the MWCNT (002) crystalline plane in coaxial fibers. The variation in PEDOT:PSS content does not have a significant effect on the orientation of the (110) crystal plane of SA in the fiber. For coaxial fibers, the high orientation of the core layer MWCNT is one of the main reasons for the high electrical conductivity. At the same time, the skin ratio in the coaxial fiber does not have a significant effect on the (002) crystal plane orientation of MWCNT in the core.

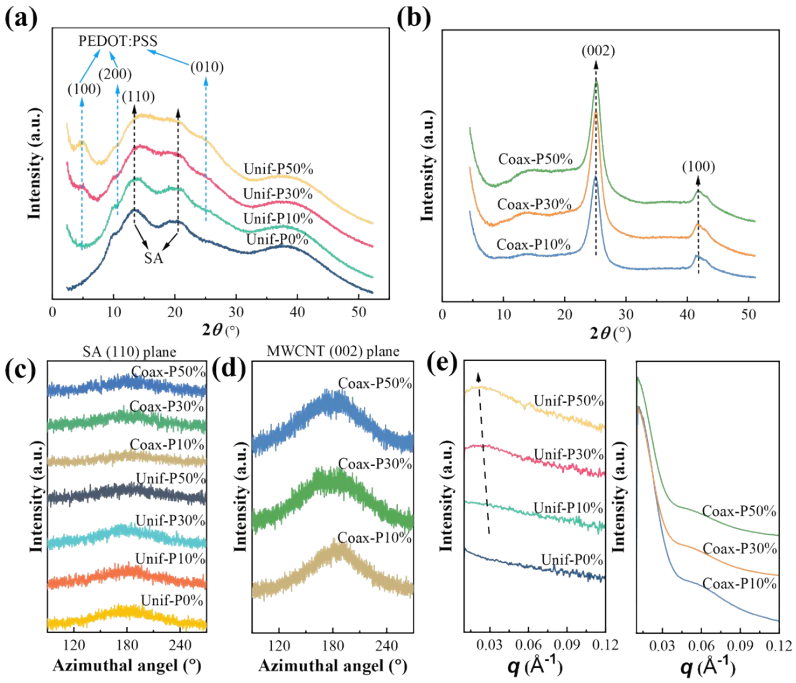

Fig. S7 1D-WAXD curves of (a) uniform fibers and (b) coaxial fibers integrated in a circular manner from the corresponding 2D-WAXD patterns in Fig. S6(a). β scan integration of the (c) SA (110) plane and (d) MWCNT (002) plane diffraction. 1D-SAXS curves of uniform fiber and coaxial fibers integrated from the corresponding 2D-SAXS patterns in Fig. S6(b). The cake integration was conducted along the (e) meridional line.

Fig. S6(b) shows the 2D-SAXS patterns of coaxial and uniform fibers. The 2D-SAXS patterns of uniform fibers show spindle-shape signal, which may be due to the fibril structure produced during the spinning process. The 2D-SAXS patterns of coaxial fibers exhibit signal in elliptical shape, indicating the orientation of fibers and the stronger MWCNT scattering signal than SA/PEDOT:PSS. The 2D-SAXS image was integrated by cake integration along the meridian direction, and the resulting 1D curve is shown in Fig. S7(e), where the scattering signal of uniform fibers shows a periodic variation with the increasing PEDOT:PSS content. The scattering signal of SA/PEDOT:PSS in coaxial fibers is masked by MWCNT. As the PEDOT:PSS content is increased, no significant change in the scattering signal of coaxial fibers can be seen.

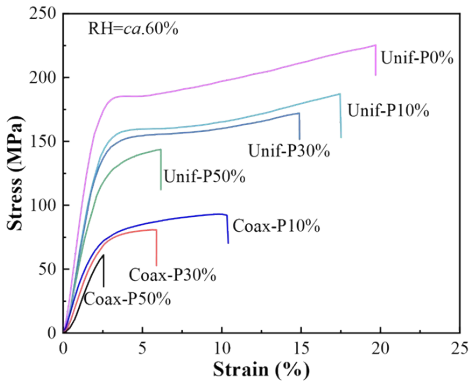

Fig. S8 Stress–strain curves of uniform and coaxial fibers at RH = *ca*. 60%.

Fig. S8 illustrates the stress-strain curves of uniform and coaxial fibers at RH = 60%. It can be seen that the tensile strength and elongation-at-break of uniform fibers decrease with the PEDOT:PSS content increases. PEDOT:PSS synthesized in this study is a granular conductive species, which has a lower tensile strength and elongation-at-break than SA. This results in the decreased mechanical properties of the uniform fibers after addition of PEDOT:PSS. The mechanical properties of the coaxial fibers are mainly contributed by the skin layer of SA/PEDOT:PSS fibers, but not the core layer of MWCNTs that without tightly entangled structure. Therefore, the mechanical properties of coaxial fibers decrease with the PEDOT:PSS content increases, which exhibits a similar tendency with the situation in uniform fibers.

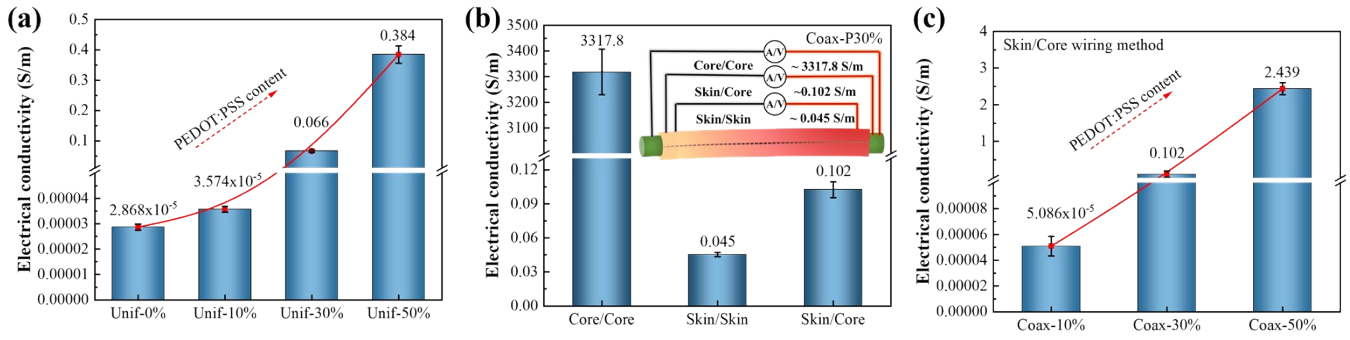

Fig. S9 (a) Electrical conductivity of uniform fibers with different PEDOT:PSS contents. (b) Electrical conductivity of Coax-P30% fibers with different wiring methods. (c) Electrical conductivity of coaxial fibers with different PEDOT:PSS contents in the “Skin/Core” wiring method.

Fig. S9(a) shows the effect of PEDOT:PSS content on the electrical conductivity of the uniform fibers. The electrical conductivity of the uniform fibers increases significantly as the PEDOT:PSS contents increase. On the one hand, the content of PEDOT:PSS will directly affect the electrical conductivity of the fiber due to the fact that PEDOT: PSS is a conductive polymer. On the other hand, with the increase of PEDOT:PSS content, the increased crystallinity of the fiber matrix makes it more conducive to electron transmission. Fig. S9(b) shows the electrical conductivities of Coax-P30% fibers under various wiring methods. The "Core/Core" wiring method has the highest electrical conductivity of Coax-P30% fibers, up to 3317.8 S/m, which is because the "Core/Core" wiring method measures essentially electrical conductivity of MWCNT. Comparing the wiring methods of "Skin/Core" and "Skin/Skin", it can be noticed that the electrical conductivity of the "Skin/Core" layer is higher. This is because the "Skin/Core" wiring allow the electron migration follow the coaxial fibers radial direction first, and then the axial direction (MWCNT), which has a lower resistance to electron migration as a whole. This low resistance migration path for electrons is caused by the skin-core structure of the coaxial fibers in this study. The electrical conductivity of coaxial fibers with different PEDOT:PSS contents in the "Skin/Core" wiring method was studied as shown in Fig. S9(c). Similarly, Coax-fibers with SA/PEDOT:PSS skin layer show the same tendency with the Uniform-fibers.

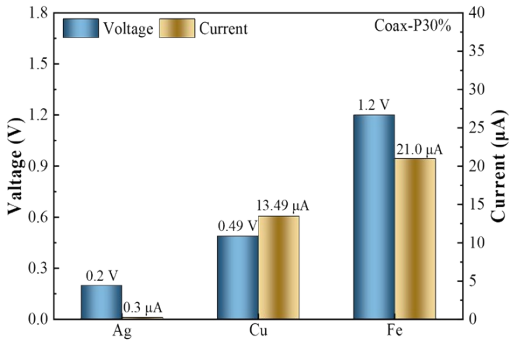

Fig. S10 Effect of metal electrodes on the maximum output voltage and current of Coax-P30% FMEG.

Changing the electrode material is also an effective way to improve the moist-electric performance. The moist-electric performance of Coax-P30% FMEG is investigated by varying external electrode due to the fact that the MWCNT core layer is used as the inner electrode material in this study. Fig. S10 illustrates the moist-electric performance of Coax-P30% FMEG with constant moisture stimulation using silver, copper and iron as the external electrodes. It can be seen that the FMEGs with iron external electrode have the best moist-electric performance. At this stage there are two claims reported about improving moist-electric performance by electrode materials. One is that the electrode material and the active material form a Schottky contact and an Ohmic contact, respectively.[8] The other is that the active electrode material interacts with water to release more free H^+ as charges, which increases the moist-electric performance due to the increase in potential between the electrodes.[9] In this study, the MWCNT core layer is the inner electrode with a work function of 5.0 eV. The work functions of silver, iron and copper are 4.3, 4.5 and 4.7 eV, respectively, with the value of iron electrode between that of silver and copper. It is clear that the electrode material does not form a Schottky and ohmic contact with the active material. The main reason for the increased moist-electric performance is that iron, as an active metal, generates positively charged cations (ferric ions) when interacting with moisture. SA and PSS in the cortex of Coax -P30% fiber are polyanion electrolytes that ionize when interacting with water, resulting in molecular chains with a large amount of anions. A charge distribution is formed in the radial direction of the coaxial fibers and counter ions will be mobile with the help of moisture.[9] This process results in a significant built-in electric field, which generates an appreciable electrical output.

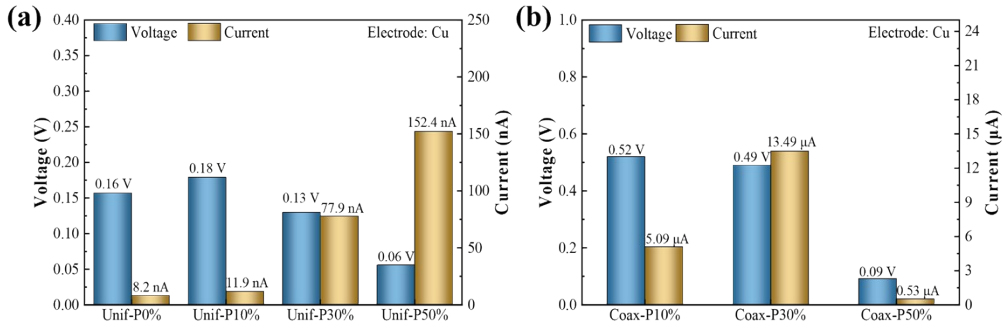

Fig. S11 Maximum output voltage and current for different ratios of (b) uniform and (c) coaxial FMEGs with Cu as outer electrode.

In order to reduce the influence of metals on the moist-electric properties, copper, an inactive metal, was chosen as the outer electrode material to investigate the effect of PEDOT:PSS content on the moist-electric properties. Fig. S11(a-b) shows the extreme values of output voltage and current under moisture stimulation for coaxial and uniform fiber based FMEGs with different SA/PEDOT:PSS ratios. It can be seen that the output voltage of uniform and coaxial FMEGs tends to increase and then decrease as the PEDOT:PSS content increases. The output current of the uniform fibers tends to increase, while the output current of the coaxial fibers tends to increase and then decrease as the PEDOT:PSS content increases. This is because PEDOT:PSS increases the electrical conductivity of the active material and reduces the resistance to charge movement, resulting in an increase of its power generation performance. At the same time the increase of PEDOT:PSS composition reduces the relative content of polar groups in the active material, resulting in a reduction in power generation performance.

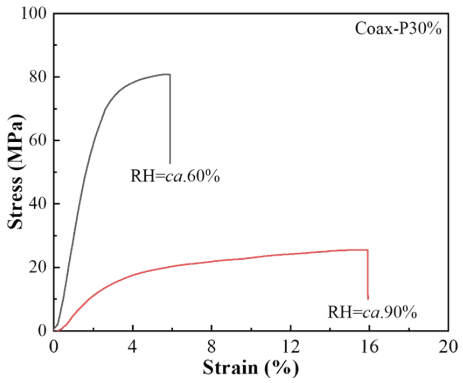

Fig. S12 Stress–strain curves of Coax-P30% fibers at RH = *ca*. 60% and RH = ca. 90%

With the increase of humidity, the intermolecular binding forces of fibers becomes weaker due to the increase of moisture content in fibers, resulting in the decrease of fiber tensile strength and increase of

elongation-at-break.

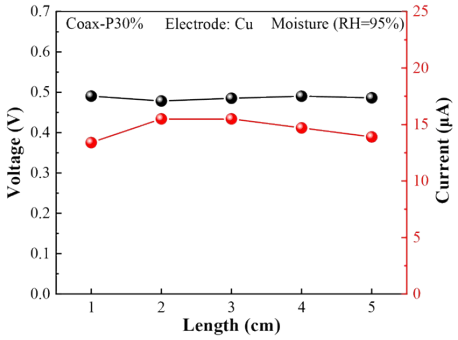

Fig. S13 Effect of FMEG length on output voltage and current

Cu was selected as the outer electrode to study the moist-electric properties of Coax-P30% FMEG with different lengths to eliminate the influence of electrodes. The voltage and current of the FMEG are relatively stable (Fig. S13) when the fiber length is within 1-5cm. The voltage generated by the FMEG depends on the potential difference between the positive and negative electrodes. The proton concentration difference generated by the interaction of skin and core layers with water is the same for Coax-fibers with different lengths in the same humidity environment, so the potential difference between the positive and negative electrodes is basically the same. The current of the FMEG is more dependent on the impedance of the material. In this study, the influence of fiber length on impedance is not a simple multiplying relationship due to the skin-core structure of the coaxial fiber. This process is complex, and the effect of longer coaxial fiber length on the moist-electric properties will be studied in detail in the next system.

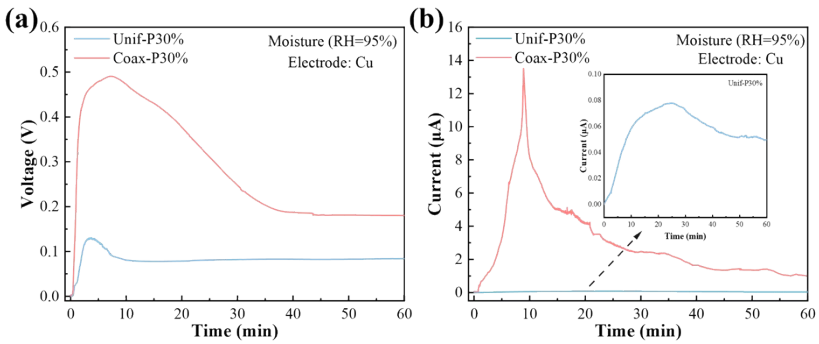

Fig. S14 Comparison of (a) output voltage and (b) current of Coax-P30% and Unif-P30% fibers under moisture stimulation (Cu electrode)

A comparison of Fig. S14(a-b) shows that the output voltage and current of Coax-P30% FMEG can be nearly *4* and *170* times of Unif-P30% FMEG, respectively, which demonstrates the advantage of coaxial

fibers in moist-electric studies.

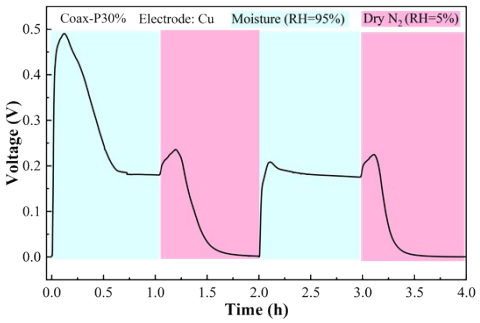

Fig. S15 Memory of the voltage of the Coax-P30% FMEG with Cu as outer electrode in response to moisture stimulation.

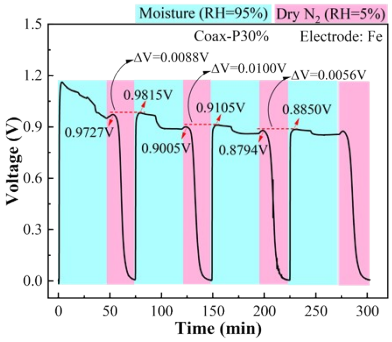

Fig. S16 Memory of the voltage of the Coax-P30% FMEG with Fe as outer electrode in response to moisture stimulation.

As illustrated in Fig. S16, voltage variation (ΔV) between the end of a moisture-dry N_2 stimulation and the starting output voltage in the next cycle depends on the drying time of the FMEG in process III. When the drying time of FMEG in process III is less than 30 min, the ΔV is only about 0.0100 V, indicating that FMWG behavior is in a memory manner. The ΔV will become greater, and the FMEG behavior will gradually change from memory to cyclability when the drying time in process III is long enough (24 h).

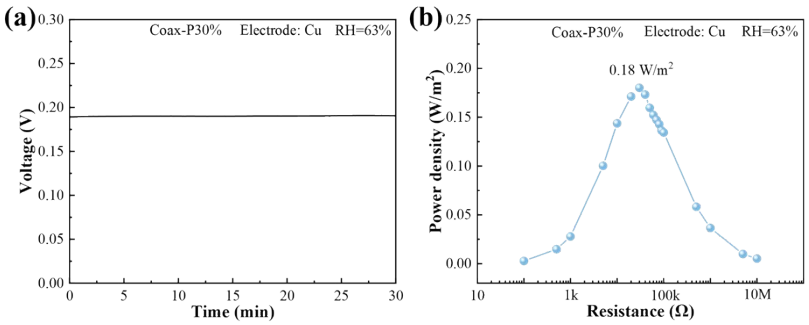

Fig. S17 (a) The output voltage of the Coax-P30% FMEG with Cu as outer electrode (RH = 63%). (b) The Output power density of the Coax-P30% FMEG with Cu as outer electrode at different loads (RH = 63%).

As illustrated in Fig. S17, the output voltage and maximum output power density of the Coax-P30% FMEG with Cu as outer electrode are 0.19 V and 0.18 W/m^2 at RH = 63%, respectively.

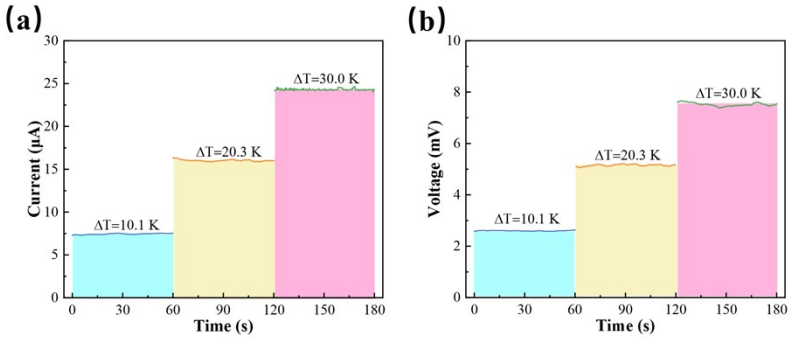

Fig. S18 (a) Output currents and (b) voltages of Coax-P30% FTEG at different Δ*T* constructed using hot plate/ambient temperatures

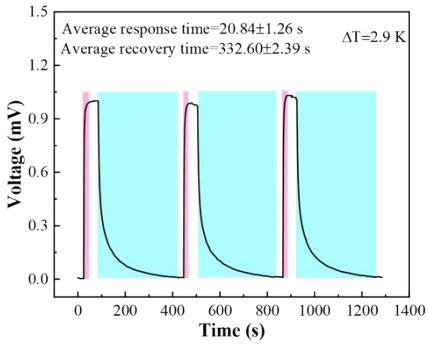

Fig. S19 Coax-P30% FTEG response and recovery time to heat at ΔT = 2.9 K.

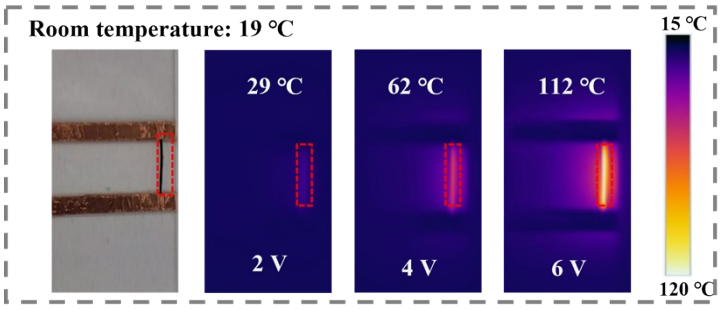

Fig. S20 Thermal infrared image of Coax-P30% at different voltages.

The infrared thermogram shows that the Coax-P30% fiber heat up uniformly at different applied

voltage (Fig. S20), which indicates the continuous uniformity of the MWCNTs in the fiber core layer.

Table S1. Electrical output of MEG in different studies

No.	Materials	Electrode	RH (%)	Voltage (V)	Current (μA)	P_{mmo} (W/m^2)	Ref.
1	PAAS/GO film	Au/Ag	80	0.60	-	7 x10^{-4}	10
2	PSS-PVA-PDDA film	C	85	1.38	1.0	5.52 x10^{-2}	11
3	GO/paper	Ag	70	0.30	0.7	0.27	12
4	Gelatin film	Cu/Al	90	0.71	-	5.52 x10^{-2}	13
5	SA/SiO2/rGO film	Au	100	0.5	100	0.12	1
6	Wood	C	Water	0.3	10	-	14
7	Protein nanofiber	Pt	99	0.11	-	6.3 x10^{-6}	15
8	Corn stalk	C	75	0.56	3.6	1.06 x10^{-3}	16
9	Cotton	C	55	0.74	22.5	-	17
10	Cellulose paper	ITO/Au	70	0.25	0.015	-	18
11	Paper-pencil	C	95	0.48	8	1.91 x10^{-3}	19
12	Fabric/carbon black	C	water	0.53	3.91	-	20
13	GO fiber	Ag	70	0.34	10.5	-	21
14	GO fiber	C	65	0.36	-	-	22
15	Cellulose/CNT fiber	Cu	water	0.16	0.17	-	23
16	FMEG	C/Cu	95	0.49	13.49	-	This work
17	FMEG	C/Cu	63	0.19	-	0.18	This work
18	FMEG	C/Fe	95	1.2	21.0	-	This work
19	FMEG	C/Fe	63	0.6-	-	5.56	This work

PAAS, PVA, PDDA, C, and ITO represent sodium polyacrylate, polyvinyl alcohol, polydiallyl dimethyl ammonium chloride, carbon, and indium tin oxide, respectively.

Table S2 Electrical output of TEG in different studies

No.	Materials	Area (cm^2)	Type	ΔT (K)	Voltage (mV)	Current (μA)	P_{Tmo} (nW/cm^2)	Ref.
1	CNT/Carbon nanoparticle	7.6	film	5	-	-	15.8	24
2	CNT/P3HT	6.15	film	10	41.8	1.6	5.31	25
3	SSWCNT/P3HT	4.2	film	10	6.2	44.2	16.26	26
4	CNT/P3HT	6.3	film	10	5.0	9.0	7.30	27
5	CNT/PEDOT:PSS	6.3	film	10	2.0	18.5	5.76	27
6	CNT/PEDOT:PSS	6.3	film	10	5.0	12.5	4.73	28
7	MWCNT/PEI	-	film	40	0.23	7.6	-	29
8	CNT/Biomolecule	21	yarn	20	4.5	-	0.44	30
9	FTEG	0.46	fiber	30	7.52	24.28	27.27	This work

P3HT, SSWCNT, and PEI represent poly(3-hexylthiophene), small-bundled single-walled carbon nanotube, and

polyethyleneimine, respectively.

Reference

1 H. Wang, T. He, X. Hao, Y. Huang, H. Yao, F. Liu, H. Chen, L. Qu, *Nat. Commun.*, 2022, **13(1)**, 1-11.

2 P. Sundarrajan, P. Eswaran, A. Marimuthu, L. B. Subhadra, P. Kannaiyan, *Bull. Korean Chem. Soc.*, 2012, **33(10)**, 3218-3224.

3 D. Zheng, B. Bai, X. Xu, Y. He, S. Li, N. Hu, H. Wang, *RSC Adv.*, 2019, **9(48)**, 27961-27972.

4 C. Larosa, M. Salerno, J. S. De Lima, R. M. Meri, M. F. Da Silva, L. B. De Carvalho, A. Converti, *Int. J. Biol. Macromol.*, 2018, **115**, 900-906.

5 E. G. Kim, J. L. Brédas, *J. Am. Chem. Soc.*, 2008, **130(50)**, 16880-16889.

6 M. Qu, H. Wang, R. Zhang, Q. Chen, Q. Zhao, R. Liu, P. Tang, Y. Bin, *Chem. Eng. J.*, 2022, 450, 138093.

7 H. Yi, H. Wang, Y. Jing, T. Peng, Y. Wang, J. Guo, Q. He, Z. Guo, X. Wang, *J. Mater. Chem. A,* 2015, **3(38)**, 19545-19555.

8 Y. Huang, H. Cheng, C. Yang, P. Zhang, Q. Liao, H. Yao, G. Shi, L. Qu, *Nat. Commun.,* 2018, **9(1)**, 1-8.

9 Z. Sun, L. Feng, X. Wen, L. Wang, X. Qin, J. Yu, *Mater. Horizons*, 2021, **8(8)**, 2303-2309.

10 Y. Huang, H. Cheng, C. Yang, H. Yao, C. Li, L. Qu, *Energy Environ. Sci.*, 2019, **12(6)**, 1848-1856.

11 H. Wang, Y. Sun, T. He, Y. Huang, H. Cheng, C. Li, D. Xie, P. Yang, Y. Zhang, L. Qu, *Nat. Nanotechnol.*, 2021, **16(7)**, 811-819.

12 Y. Liang, F. Zhao, Z. Cheng, Y. Deng, Y. Xiao, H. Cheng, P. Zhang, Y. Huang, H. Shao, L. Qu, *Energy Environ. Sci.*, 2018, **11(7)**, 1730-1735.

13 S. Mandal, S. Roy, A. Mandal, T. Ghoshal, G. Das, A. Singh, D. K. Goswami, *ACS Appl. Electron. Mater.*, 2020, **2(3)**, 780-789.

14 X. Zhou, W. Zhang, C. Zhang, Y. Tan, J. Guo, Z. Sun, X. Deng, *ACS Appl. Mater. Interfaces*, 2020, **12(9)**, 11232-11239.

15 M. Li, L. Zong, W. Yang, X. Li, J. You, X. Wu, Z. Li, C. Li, *Adv. Funct. Mater.*, 2019, **29(32)**, 1901798.

16 F. Gong, H. Li, Q. Zhou, M. Wang, W. Wang, Y. Lv, R. Xiao, D. V. Papavassiliou, *Nano Energy*, 2020, **74**, 104922.

17 J. Bae, T. G. Yun, B. L. Suh, J. Kim, I. Kim, *Energy Environ. Sci.*, 2020, **13(2)**, 527-534.

18 X. Gao, T. Xu, C. Shao, Y. Han, B. Lu, Z. Zhang, L. Qu, *J. Mater. Chem. A*, 2019, **7(36)**, 20574-20578.

19 Y. Xu, G. Zhao, L. Zhu, Q. Fei, Z. Zhang, Z. Chen, F. An, Y. Chen, Y. Ling, P. Guo, S. Ding, G.

Huang, P. Chen, Q. Cao, Z. Yan, *Proc. Natl. Acad. Sci. U.S.A.*, 2020, **117(31)**, 18292-18301.

20 Y T. G. Yun, J. Bae, A. Rothschild, I. Kim, *ACS nano*, 2019, **13(11)**, 12703-12709.

21 C. Shao, J. Gao, T. Xu, B. Ji, Y. Xiao, C. Gao, Y. Zhao, L. Qu, *Nano Energy*, 2018, **53**, 698-705.

22 Y. Liang, F. Zhao, Z. Cheng, Q. Zhou, H. Shao, L. Jiang, L. Qu, *Nano Energy*, 2017, **32**, 329-335.

23 J. Chen, Y. Li, Y. Zhang, D. Ye, C. Lei, K. Wu, Q. Fu, *Adv. Funct. Mater.*, 2022, **32**, 2203666.

24 W. Park, H. Hwang, S. Kim, S. Park, K. Jang, *ACS Appl. Mater. Interfaces*, 2021, **13(6)**, 7208-7215.

25 C. T. Hong, Y. H. Kang, J. Ryu, S. Y. Cho, K. Jang, *J. Mater. Chem. A*, 2015, **3(43)**, 21428-21433.

26 Y. Kang, U. Lee, I. H. Jung, S. Yoon, S. Cho, *ACS Appl. Electron. Mater.*, 2019, **1(7)**, 1282-1289.

27 W. Lee, Y. H. Kang, J. Y. Lee, K. Jang, S. Y. Cho, *Mater. Today Commun.*, 2017, **10**, 41-45.

28 W. Lee, Y. H. Kang, J. Y. Lee, K. Jang, S. Y. Cho, *RSC Adv.*, 2016, **6(58)**, 53339-53344.

29 M. Bharti, A. Singh, B. P. Singh, S. R. Dhakate, G. Saini, S. Bhattacharya, A. K. Debnath, K. P. Muthe, D. K. Aswalac, *J. Power Sources*, 2020, **449**, 227493.

30 Y. Cho, N. Okamoto, S. Yamamoto, S. Obokata, K. Nishioka, H. Benten, M. Nakamura, *ACS Appl. Energy Mater.*, 2022, **5**, 3698.